CHEMISTRY OF MATERIALS
Cite This: *Chem. Mater.* 2018, 30, 8811−8821
Article
pubs.acs.org/cm

Shear-Assisted Formation of Cation-Disordered Rocksalt $NaMO_2$ (M = Fe or Mn)

Tan Shi,[†,‡] Penghao Xiao,[‡] Deok-Hwang Kwon,[†] Gopalakrishnan Sai Gautam,[‡] Khetpakorn Chakarawet,[§] Hyunchul Kim,[‡] Shou-Hang Bo,[*,‡,∥] and Gerbrand Ceder[*,†,‡]

[†]Department of Materials Science and Engineering, University of California, Berkeley, California 94720, United States
[‡]Materials Sciences Division, Lawrence Berkeley National Laboratory, Berkeley, California 94720, United States
[§]Department of Chemistry, University of California, Berkeley, California 94720, United States
[∥]University of Michigan-Shanghai Jiao Tong University Joint Institute, Shanghai Jiao Tong University, 800 Dongchuan Road, Minhang District, Shanghai 200240, P. R. China

Supporting Information

ABSTRACT: We report the synthesis of cation-disordered rocksalt $NaMO_2$ (M = 3d transition metal), i.e., $NaFeO_{2-\delta}$ ($\delta \sim 0.18$), for the first time via a martensitic-like phase transformation from β-$NaFeO_2$. This disordered rocksalt $NaFeO_{2-\delta}$ does not exhibit long-range cation ordering, as evidenced by synchrotron X-ray diffraction, neutron diffraction, and transmission electron microscopy analyses. Pair distribution function analysis revealed that although the cation sublattice mostly preserved the rocksalt symmetry, O atoms were significantly displaced to accommodate the different Na^+−O, Fe^{2+}−O, and Fe^{3+}−O bond lengths (~2.4, 2.1, and 2 Å, respectively). In addition, we confirmed the presence of O vacancies and partial Fe reduction from 3+ to 2+ in $NaFeO_{2-\delta}$ based on ^{57}Fe Mössbauer and X-ray absorption spectroscopy analyses. Controlled experiments revealed that three factors are essential for the successful synthesis of the rocksalt structure: (1) an appropriate precursor structure, (2) the application of a large stress by high-energy milling, and (3) the creation of O vacancies via carbon reduction. Density functional theory calculations demonstrated that these factors substantially affect the energetics of the minimum-energy reaction path of the phase transformation, making the highly metastable disordered rocksalt phase accessible. Our work suggests the effectiveness of mechanical milling to access metastable phases that are structurally related to the precursors via a shearing transformation. Utilizing this mechanism, we were able to predict and synthesize another cation-disordered rocksalt structure, $NaMnO_2$, and explain the syntheses of several other related materials.

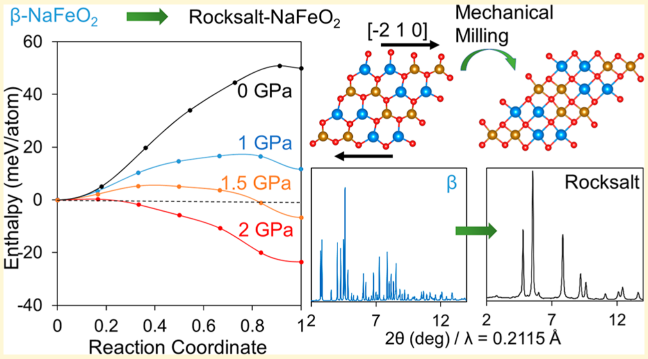

INTRODUCTION

Materials discovery plays a central role in scientific and technological developments. The synthesis of new materials with tailored properties has been a long-standing challenge in materials and chemistry research. Although precise control can now be achieved at the molecular or framework level (e.g., covalent organic frameworks) for the synthesis of organic solids,[1] the synthesis of inorganic materials is often still performed using a trial-and-error approach and is often limited to thermodynamically stable phases. Metastable inorganic materials (which are kinetically trapped in states with energies above the lowest-energy ground states) can sometimes exhibit superior properties compared to those of their stable counterparts, thereby finding applications in a broad variety of technologies.[2−4] However, a comprehensive understanding of the governing chemical and physical principles for the formation of metastable materials is lacking, making predictive synthesis impossible.

With the advent of large databases that contain well-computed properties of materials, such as the Materials Project and the like,[5,6] one can now analyze the thermodynamic properties of almost any experimentally reported inorganic crystalline material and rationalize the criteria for the formation of metastable materials. The findings of a recent data-mining effort suggested that the magnitude of the energy above the ground state is not the only measure that determines if a metastable phase can be synthesized;[7] i.e., not all low-energy metastable compounds can be synthesized. Rather, a synthesizable metastable compound must be the lowest free-energy phase under certain thermodynamic conditions during the synthesis and must be retained until ambient conditions are reached, leading to the hypothesis of "remnant

Received: August 16, 2018
Revised: October 15, 2018
Published: November 21, 2018

DOI: 10.1021/acs.chemmater.8b03490
Chem. Mater. 2018, 30, 8811−8821

metastability". The concept of remnant metastability underscores the importance of constructing the energy landscape of materials not only under typically applied thermodynamic conditions (e.g., temperature and pressure) but also under shear stresses and for various compositions, among other conditions. This complex energy landscape can potentially lead to the identification of the thermodynamic conditions under which a metastable material would be the lowest free-energy phase and the prediction of a viable synthesis route. This approach has recently been applied in a number of cases to successfully explain the structure selection rules of polymorphic materials under various synthesis conditions.[7−9]

Among all the available thermodynamic handles, temperature and pressure are the most commonly used to synthesize metastable materials but have limited applicability. The experimental synthesis of metastable phases via the traditional solid-state chemistry route is difficult because there is a thermodynamic driving force for the system to progress toward the free-energy minimum, particularly at high synthesis temperatures and slow cooling rates. New solid phases can also be synthesized through the control of pressure.[10] However, this process often requires an extremely high pressure apparatus, mostly because of the small volume variations between the solid-state reagents and products, which limits the scalability of such methods.[11]

Shear stress provides an additional handle, which makes mechanochemistry a promising method for the synthesis of metastable materials. During mechanical milling, the materials experience large mechanical stresses on the scale of gigapascals and local heating up to ∼800 K.[12] More importantly, the stress applied by milling has large shear components, which can accelerate some reactions by several orders of magnitude.[12−14] Compared with high-pressure synthesis, mechanical milling not only drives reactions toward the direction of volume shrinkage via compression but also reduces the energy barriers along shear directions, providing a new route for tuning chemical reactions. Mechanical milling also ensures intimate mixing of all the components at all times and continuously creates surface and bulk defects.[15] All of these factors increase the probability of the system accessing metastable states.

Using mechanochemistry, we have successfully synthesized a new highly metastable polymorph of $NaFeO_2$ (i.e., a cation-disordered rocksalt structure). Extensive research has been performed on $NaFeO_2$ since the 1970s because of its potential use as a Na intercalation cathode and its intriguing magnetic properties. Three polymorphs of $NaFeO_2$ have been previously reported (α, β, and γ).[16−18] α-$NaFeO_2$ is the ground state and is stable under ambient conditions. The β and γ phases are considered high-temperature phases and are stable above 760 and 1010 °C, respectively.[17,18] α-$NaFeO_2$ adopts a cubic-close-packed oxygen array, whereas the β and γ polymorphs possess a hexagonal-close-packed oxygen sublattice. α-$NaFeO_2$ (space group $R\bar{3}m$) has a layered structure, where all the octahedral sites are occupied by cations (i.e., Na^+ and Fe^{3+}) and Na−O and Fe−O slabs alternate along the c lattice direction.[18] β-$NaFeO_2$ (space group $Pna2_1$) has an ordered wurtzite structure, where all the T+ tetrahedral sites are occupied by Na and Fe cations, leaving all the T− and octahedral sites vacant ("T+" and "T−" denote tetrahedra with opposite pointing directions).[17] γ-$NaFeO_2$ (space group $P4_12_12$) is topotactically related to β-$NaFeO_2$. However, in the high-temperature γ structure, half of the cations are moved to the neighboring T− tetrahedral sites (while maintaining the cation ordering).[17] It is important to note that because of differences in the ionic radii and valence states, Na and Fe do not share crystallographic sites in any of the three $NaFeO_2$ polymorphs, resulting in Na−O and Fe−O polyhedra with distinct bond distances (∼2.3−2.4 Å for Na−O and ∼1.8−2.1 Å for Fe−O).

In this article, we present for the first time the synthesis, structure, and formation mechanism of cation-disordered rocksalt $NaFeO_2$, which was produced via a martensitic-like phase transformation from β-$NaFeO_2$ (i.e., the phase transition mostly involves homogeneous lattice distortion and not atomic diffusion). The formation of this cation-disordered rocksalt phase is surprising considering that Na and Fe cations share the same crystallographic site and, therefore, the same metal−oxygen coordination geometry in the average structure. Indeed, on the basis of our calculations, the energy of this cation-disordered polymorph is 132 meV/atom higher than that of α-$NaFeO_2$, which is far beyond the normal energy range of most observed metastable materials (<70 meV/atom above ground-state phases).[7,19] Note that the synthesis of the cation-disordered $NaFeO_2$ structure requires the simultaneous use of a specific precursor (β-$NaFeO_2$ and not α-$NaFeO_2$), a reducing agent (carbon), and mechanical milling, which suggests that each of these synthesis conditions plays a crucial role in producing this metastable phase.

Below, we first describe the structure of cation-disordered rocksalt $NaFeO_2$, followed by a discussion of the β-$NaFeO_2$-to-rocksalt $NaFeO_2$ phase transformation mechanism. Synchrotron X-ray diffraction (XRD) and pair distribution function (PDF) analysis were used to investigate the bulk and local structures of $NaFeO_2$. The Fe oxidation state and Fe−O coordination geometry in rocksalt $NaFeO_2$ were probed using ^{57}Fe Mössbauer spectroscopy and X-ray absorption spectroscopy (XAS) analysis. Together with a transmission electron microscopy (TEM) study, these results provide a precise and comprehensive description of the structure of $NaFeO_2$, suggesting the presence of large local distortions and O vacancies in the rocksalt $NaFeO_2$. The atomistic phase transformation mechanism from β-$NaFeO_2$ to rocksalt $NaFeO_2$ was examined using solid-state nudged elastic band (SSNEB) calculations, which clarified the effects of shear stress and the O vacancy defect concentration on the minimum-energy path of this phase transition. On the basis of the proposed phase transformation mechanism, we were able to predict and successfully synthesize a new disordered rocksalt $NaMnO_2$ structure in a similar fashion and explain the synthesis of other related materials. We propose that through the manipulation of shear stress and material composition (in this case, the O vacancy concentration), which is possible in mechanochemistry, a wide variety of inorganic metastable materials can be synthesized.

■ RESULTS

Structure of the Disordered Rocksalt $NaFeO_2$. The bulk and local structures of the as-prepared $NaFeO_2$ obtained by ball milling β-$NaFeO_2$ with carbon were examined using a combination of synchrotron X-ray diffraction, PDF analysis, Mössbauer spectroscopy, X-ray absorption near-edge structure (XANES) analysis, extended X-ray absorption fine structure (EXAFS), and high-resolution TEM (HRTEM). Even though the long-range averaged structure was determined to possess the rocksalt symmetry with the presence of O vacancies, large distortions were present locally.

The averaged structure of the as-prepared $NaFeO_2$ was first characterized using synchrotron XRD (Figure 1a). The $NaFeO_2$ phase was modeled very well using a simple rocksalt structure (space group $Fm\bar{3}m$) with Fe and Na atoms at the 4a site, each with an occupancy of 0.5, and an O atom at the 4b site with an occupancy of 1. The quality of the refinement was improved (2.82 vs 2.90 in R_{wp}) when the occupancy of the O 4b site was freely refined. The refined O occupancy was 0.96, suggesting that O vacancies are present in $NaFeO_2$; this conclusion was also supported by X-ray PDF analysis (Figure 1b−d) and neutron scattering measurements (Figure S1). The lattice parameter of the rocksalt $NaFeO_2$ is 4.37 Å, which is slightly larger than that of rocksalt FeO (a = 4.31 Å); this finding is consistent with the presence of the larger Na ions in the structure. In addition to the rocksalt phase, a small amount of residual β-$NaFeO_2$ (~4%, space group $Pna2_1$) and Fe metal (~1%, space group $Im\bar{3}m$) were also detected. The Fe metal was likely produced by the local heating during ball milling, leading to the reduction of $NaFeO_2$ by carbon. Indeed, thermogravimetric analysis revealed that when mixed with carbon, $NaFeO_2$ is reduced to Fe metal at approximately 750 °C (Figure S2a). TEM images revealed that nanosized $NaFeO_2$ (~10 nm) particles were embedded in a carbon matrix (Figure S3c,d). The rocksalt symmetry was confirmed by polycrystalline electron diffraction patterns and a fast Fourier-transformed (FFT) image of a single grain (Figure S3e−g).

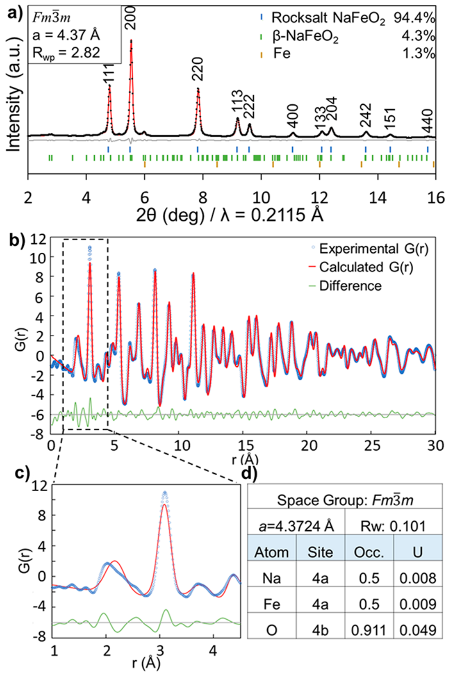

Space Group: $Fm\bar{3}m$			
a=4.3724 Å		Rw: 0.101	
Atom	Site	Occ.	U
Na	4a	0.5	0.008
Fe	4a	0.5	0.009
O	4b	0.911	0.049

Figure 1. Structure of the as-synthesized cation-disordered rocksalt $NaFeO_2$. (a) Rietveld-refined synchrotron XRD pattern of the as-prepared cation-disordered rocksalt $NaFeO_2$ with a small amount of Fe impurity and residual β-$NaFeO_2$. Detailed Rietveld refinement results are listed in Table S1. (b) Fit of X-ray PDF data of the as-synthesized rocksalt $NaFeO_2$ using the ideal cation-disordered rocksalt structure. The calculated $G(r)$ uses fitting parameters optimized for the 5−30 Å range. (c) Close-up view of first two peaks. (d) PDF fitting parameters.

Although the averaged structure of the as-prepared $NaFeO_2$ is well described as a rocksalt, our PDF analysis suggests the presence of strong local distortions. The PDF data were fitted using an ideal cation-disordered rocksalt $NaFeO_2$ structure (the same structure as that used for the Rietveld refinement) (Figure 1b). The long-range portion (5−30 Å) of the data is first fit and shows excellent agreement with the model structure, which confirms that the bulk material indeed has a cation-disordered rocksalt structure. Upon extension of the fit range (without changing the fitting parameters) to include the short-range peaks (<5 Å) corresponding to the shortest cation−anion and cation−cation (or anion−anion) distances in the rocksalt structure, the difference between the calculated and observed results becomes more pronounced. This difference, however, cannot be explained by the presence of amorphous side products or impurities, because the presence of impurities will induce large deviations in integrated intensities from the model structure in the short-range peaks.[20] Instead, the difference is mostly manifested in the asymmetry of the first peak (~2 Å), which corresponds to the Na−O and Fe−O correlations. This result suggests that instead of having a well-defined nearest-neighbor cation−anion bond distance, there is a wide distribution of distances, indicating the presence of different cation−anion bond lengths and large local distortions. The second peak (~3 Å), which mainly represents cation−cation correlation (Na−Na, Fe−Fe, and Fe−Na because the scattering contribution of O−O is much smaller), is fit relatively well despite the small difference in intensity, which might be due to short-range cation−cation orderings deviating from a completely random distribution. This result suggests that the cations are relatively close to their ideal positions. The analysis of the short-range (<5 Å) atomic correlations suggests that the local distortion caused by the different bonding requirements of Na and Fe in the $NaFeO_2$ structure is mainly realized through the displacements of the O atoms. This conclusion is also reflected in the large isotropic atomic displacement parameter (U) required for O atoms in the PDF data fitting (Figure 1d). Approximately 9% O vacancies were also detected in the PDF analysis, which is consistent with our XRD and neutron diffraction results.

The presence of O vacancies determined from the XRD/neutron scattering data indicates that some of the Fe^{3+} ions from the initial β structure are likely reduced to maintain charge neutrality in $NaFeO_{2-\delta}$ (δ ~ 0.18). To investigate partial Fe^{3+} reduction, Fe K-edge XANES spectrum was used to characterize the Fe valence state in the as-synthesized rocksalt $NaFeO_2$ structure (Figure 2a). Compared with the edge positions of the two reference materials (FeO and Fe_2O_3) with 2+ and 3+ oxidation states, it is clear that the Fe in $NaFeO_2$ is in a mixed valence state between Fe^{2+} and Fe^{3+}. The Fe^{2+} concentration is estimated to be ~32% using the linear combination method (Figure S4), corresponding to ~8% O vacancies assuming a composition of $NaFeO_{2-\delta}$, which is similar to the result obtained from PDF analysis. A quantitative analysis of the EXAFS spectrum to probe the local environment around Fe ions (Figure 2b) gives first- and second-shell coordination numbers close to 6 and 12, respectively, consistent with a rocksalt structure model with the majority of the Fe ions in octahedral coordination. The asymmetry in the peaks, particularly in the peak corresponding to the first coordination shell (Fe−O bonds), requires several different bond paths to achieve a reasonable curve fitting (Table S4). This result is highly consistent with our PDF analysis and further corroborates the existence of large local distortion.

^{57}Fe Mössbauer spectroscopy is particularly sensitive to the valence state and local environments of Fe. The parameters

DOI: 10.1021/acs.chemmater.8b03490
Chem. Mater. 2018, 30, 8811−8821

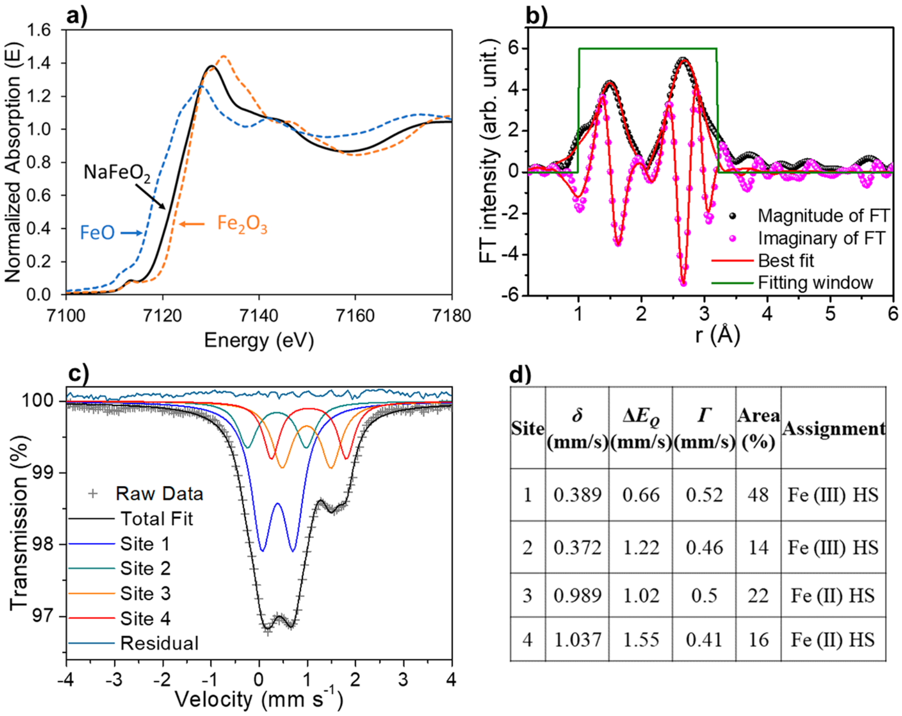

Site	δ (mm/s)	ΔE_Q (mm/s)	Γ (mm/s)	Area (%)	Assignment
1	0.389	0.66	0.52	48	Fe (III) HS
2	0.372	1.22	0.46	14	Fe (III) HS
3	0.989	1.02	0.5	22	Fe (II) HS
4	1.037	1.55	0.41	16	Fe (II) HS

Figure 2. Fe valence in the as-synthesized cation-disordered rocksalt $NaFeO_2$. (a) XANES spectra showing the Fe K edge of the as-synthesized disordered rocksalt $NaFeO_2$ with FeO and Fe_2O_3 as reference materials. (b) EXAFS fitting result for the as-synthesized disordered rocksalt $NaFeO_2$. Detailed curve fitting results for the EXAFS spectrum are shown in Table S4. (c) Room-temperature ^{57}Fe Mössbauer spectra for as-synthesized disordered rocksalt $NaFeO_2$. Sites 1 and 2 are assigned to Fe^{3+}, and sites 3 and 4 are assigned to Fe^{2+}. (d) Fitting parameters for all the components used for panel b.

[chemical shift (δ) and quadruple splitting (ΔE_Q)] of different iron species extracted by fitting the spectrum can yield important insights into the oxidation state and coordination environment of each iron center. Figure 2b presents the room-temperature (290 K) zero-field Mössbauer spectrum of $NaFeO_2$, which exhibits a complex absorption profile. The spectrum cannot be fit simply to an α-$NaFeO_2$ phase,[21] suggesting that the valence and local environment of the iron centers are more complex than in an ideal rocksalt structure, the results of which are consistent with the PDF analysis. The spectrum was satisfactorily fit employing four different iron species. Two high-spin Fe^{3+} sites were observed with isomer shifts of 0.389(6) and 0.372(10) mm/s. These values are close to the isomer shift of α-$NaFeO_2$ (0.36 mm/s),[21] thus implying Fe^{3+} is in a similar electronic environment. It should be noted, however, that the larger quadrupole splittings of 0.66(2) and 1.22(5) mm/s, respectively, as compared to those of the rocksalt structure ($\Delta E_Q = 0.50$ mm/s) might be an indication that the Fe^{3+} coordination environments are distorted from the octahedral geometry found in α-$NaFeO_2$, as evidenced by the large local distortion observed from PDF and EXAFS data. In addition, an absorption profile corresponding to high-spin Fe^{2+} could be observed. A satisfactory fit was achieved when two additional high-spin Fe^{2+} sites were included, with isomer shifts of 0.989(7) and 1.037(7) mm/s and quadrupole splittings of 1.02(3) and 1.55(3) mm/s. All parameters are consistent with what was expected for typical Fe^{3+} or Fe^{2+} found in related materials.[21,22] We determined that the concentration of Fe^{2+} in the material is ~38%, corresponding to ~9% O vacancies, which is consistent with the PDF and XANES results. The fact that four different Fe environments are needed to achieve a relatively good fit can be justified by examining the Fe environments in the relaxed DFT rocksalt structure with 6% O vacancies (Figure S5). The two lowest-O vacancy arrangements were considered. For both of these, we found at least two different Fe^{2+} environments (resembling tetrahedral and square pyramidal coordination) and two Fe^{3+} environments (resembling octahedral and square pyramidal coordination) (Figure S5b).

Rocksalt Phase Formation Mechanism. A mechanism for the β-$NaFeO_2$-to-rocksalt $NaFeO_2$ phase transformation is presented in this section. We will show that the particular structure of the precursor (β-$NaFeO_2$), the shear stress provided by mechanical milling, and the presence of carbon during milling are all required for the transformation to occur. Furthermore, using a combination of DFT computations, *ex situ* Bragg diffraction, and electron microscopy, we provide a macroscopic and microscopic description of the structural transformation process. Macroscopically, *ex situ* Bragg diffraction shows the phase transformation primarily involves only two phases (the β and disordered rocksalt phases and no other intermediates). Microscopically, TEM data suggest the transformation was initiated on the surface (~20 nm) of the β-$NaFeO_2$ particles, where a high concentration of stacking faults is observed.

First, we note that the rocksalt phase $NaFeO_2$ can be produced only when β-$NaFeO_2$ is ball milled. Although α-$NaFeO_2$ has the same chemical composition, it does not transform into the rocksalt structure under the same milling conditions (Figure S2c). The different responses to mechanical shear stress suggest that the transformation of β-$NaFeO_2$ to rocksalt $NaFeO_2$ may be facilitated by a structural relation. Indeed, β-$NaFeO_2$ has a distorted ordered wurtzite structure, and wurtzite-to-rocksalt transitions have been previously

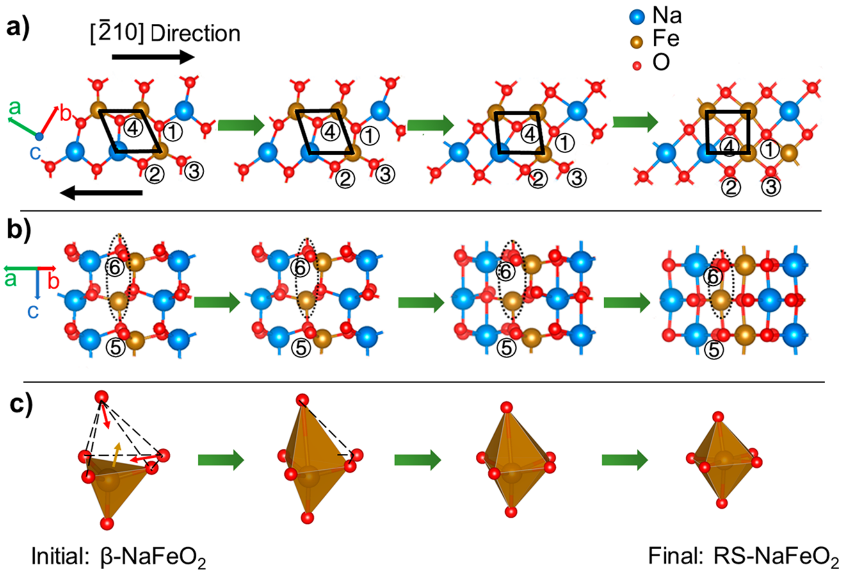

Figure 3. Snapshots of the structure along the MEP of the β-NaFeO$_2$-to-rocksalt NaFeO$_2$ transformation calculated with DFT forces. (a and b) Top and side views, respectively, of the structure during the phase transition. (c) Local environment of an Fe atom during the transition.

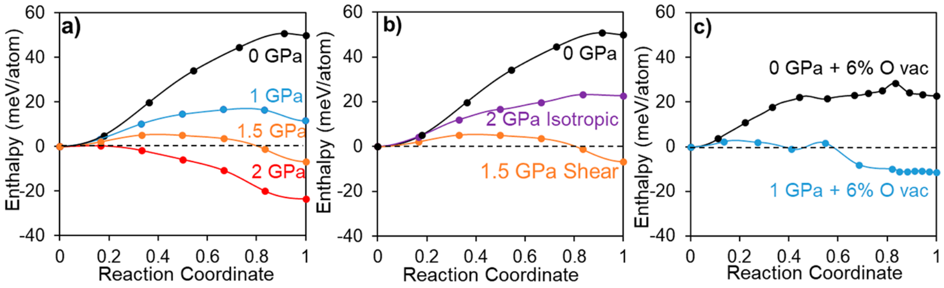

Figure 4. Minimum-enthalpy paths for the β-NaFeO$_2$-to-rocksalt NaFeO$_2$ phase transition under different stresses. (a) Minimum-enthalpy paths under shear stresses applied along the [$\bar{2}$10] direction (the atomic configurations along the path are shown in Figure 3). (b) Comparison of the change in the enthalpy barriers for the β to rocksalt phase transition under isotropic pressure and shear stress. Shear stress is shown to be much more efficient in lowering the barrier. (c) Minimum-enthalpy paths under the same shear stress with 6% O vacancies.

observed for many binary compounds.[23−25] Molecular dynamics simulations[26] and SSNEB studies[27,28] all show that binary compounds with the wurtzite structure, such as CdSe, can be transformed under pressure to a rocksalt structure via a shearing mechanism, which mostly involves collective lattice distortion rather than atomic diffusion. A similar diffusionless shear deformation could bring β-NaFeO$_2$ to rocksalt NaFeO$_2$, in which the cation ordering of β-NaFeO$_2$ is preserved in the rocksalt framework. The minimum-energy path (MEP) for this phase transformation is calculated by the SSNEB method with DFT forces. Figure 3 consists of several snapshots of the structure along the MEP and shows how the structure of the β phase can transform into the ordered rocksalt structure through a shear deformation. The shear is along the [$\bar{2}$10] direction on the (210) plane (different from the close-packed stacking plane) of the β-NaFeO$_2$ framework. This direction was determined to be the direction with the lowest reaction barrier when converting the ordered wurtzite into the ordered rocksalt NaFeO$_2$ based on an analysis similar to that performed in a previous study of the CdSe wurtzite-to-rocksalt transformation.[28] Figure 3a shows the atomic arrangement within the shearing plane (210). The black lines in Figure 3a highlight the change in relative cation positions during the transformation, revealing the shear nature of the deformation. The oxygen sublattice follows the same shear deformation, as highlighted by the four oxygen atoms labeled 1−4. The detailed shearing process can be best understood by following the coordination change of the cations (Fe or Na). From the β to rocksalt phase, the cation coordination changes from 4-fold (tetrahedral) to 6-fold (octahedral), forming two additional bonds with O in the process. In the starting ordered wurtzite structure, three O atoms (labeled 1−3 in Figure 3a) within the shearing plane are bonded to an Fe (or Na) atom, forming a close-to-perfect equilateral triangle. During the shearing process, this triangle is distorted. The primary effect of this distortion is that the O atom on the top left (labeled 4 in Figure 3a) is shifted to the right, bringing it close enough to form a bond with the Fe atom. At the end of the structural transformation, a new Fe−O bond is formed, and these four bonding O atoms together form the basal square plane of an octahedron. The second Fe−O (Fe and oxygen 6) bond formation process is illustrated in Figure 3b, which presents a side view of the shearing plane (rotated 90° with respect to the [$\bar{2}$10] direction). Figure 3c tracks the local coordination environment of a single Fe atom during the transformation process, showing only the Fe atom and the six surrounding O atoms (labeled 1−6 in Figure 3a,b) during the transformation. The distance between the Fe atom and the two initially unbonded O atoms decreases, allowing the cation environment

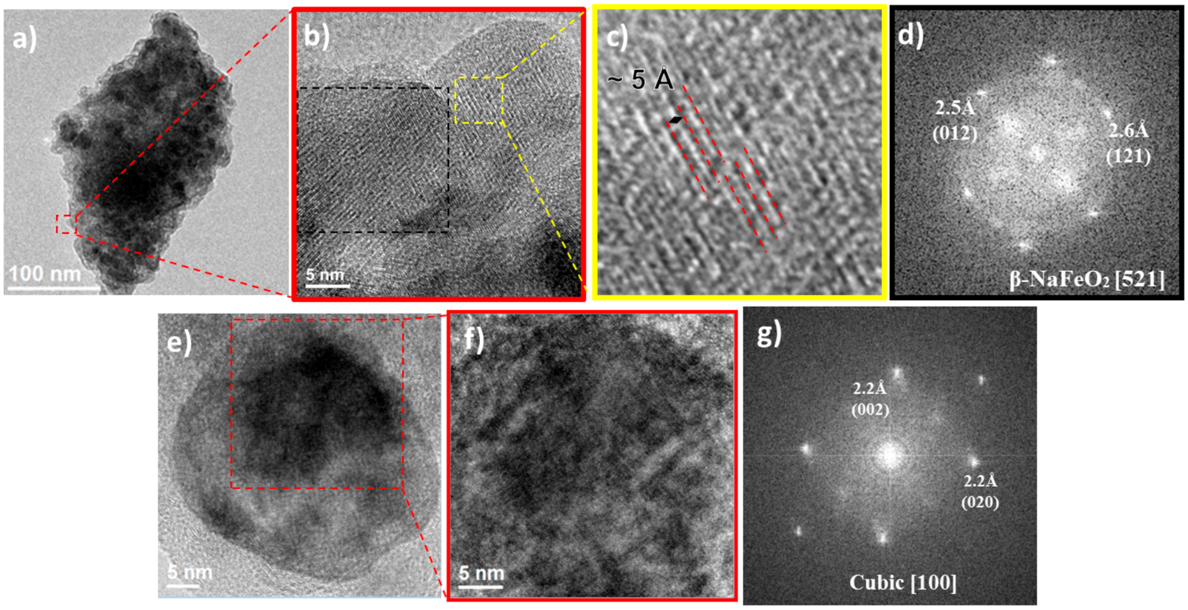

Figure 5. HRTEM images of large and small particles in the 3 h ball milled β-$NaFeO_2$ sample. (a−c) HRTEM images of a large particle (>100 nm) in the 3 h ball milled β-$NaFeO_2$ sample at different magnifications. The red dashed lines in panel c highlight the shift of the lattice fringes at the stacking fault. (d) FFT image of the area in the black square in panel b. (e and f) HRTEM images of a small particle (~30 nm) in the 3 h ball milled β-$NaFeO_2$ sample. (g) FFT image of the image in panel f.

to transform from tetrahedral to octahedral without breaking the originally present cation−anion bonds.

Second, the efficacy of mechanical milling in producing rocksalt $NaFeO_2$ can be explained by the presence of large shear stresses during the milling process. Figure 4 shows the SSNEB-calculated minimum-enthalpy paths for the phase transition depicted in Figure 3 under various conditions. Because this diffusionless phase transition requires the collective motion of thousands of atoms, the energy barrier per atom must be close to zero for the transition to occur on the macroscopic scale. When no shear stress is applied, the SSNEB calculation predicts a large barrier (51 meV/atom) for the phase transformation from the β-$NaFeO_2$ to the rocksalt structure (Figure 4a, black curve), whereas the reverse barrier needed to trap the metastable end point is small (0.87 meV/atom). Therefore, simply heating and quenching β-$NaFeO_2$ cannot be used to access the highly metastable rocksalt phase.[17,18] In addition, isotropic pressure is not effective in inducing such a phase transition. On the basis of our calculations, even at a hydrostatic pressure of 2 GPa, the transition barrier remains >20 meV/atom (Figure 4b). However, the SSNEB calculations indicate that shear stress along the $[\bar{2}10]$ direction (defined in the β-$NaFeO_2$ crystal system) can greatly reduce the transformation barrier (Figure 4a) and stabilize the rocksalt product. Under a shear stress of 2 GPa, the transition becomes nearly barrierless (Figure 4a, red curve).

Finally, we discuss the critical role of oxygen vacancies in stabilizing the metastable rocksalt. The experimental data (PDF, XANES, and Mössbauer) suggest the existence of a large amount of O vacancies (~9%) in the as-synthesized rocksalt $NaFeO_2$. Ball milling β-$NaFeO_2$ without carbon does not produce rocksalt $NaFeO_2$ and instead results in largely unchanged β-$NaFeO_2$ with a smaller particle size and a small amount of α-$NaFeO_2$, which is likely produced by the elevated temperature during ball milling (Figure S2d). In contrast, the rocksalt phase appears when as little as 5 wt % carbon is added during ball milling (Figure S2e). Clearly, the O vacancies created during the ball milling with carbon are crucial for the β-$NaFeO_2$-to-rocksalt transformation.

The DFT and SSNEB results indicate that the presence of O vacancies reduces the energy barrier for the phase transformation and lowers the energy of the rocksalt phase with respect to β-$NaFeO_2$. Our calculations show that the rocksalt structure has O vacancy formation energies lower than those of both β- and α-$NaFeO_2$ and is likely to accommodate more of these defects (Table S2). With an increasing O vacancy concentration, the energy difference between β-$NaFeO_2$ and rocksalt $NaFeO_2$ decreases (Table S3). Consequently, the SSNEB calculations indicate a reduced energy barrier for the phase transformation in the presence of O vacancies, and the shear stress required to approach a barrierless transformation is greatly reduced (~1 GPa vs 2 GPa without O vacancies), as shown in Figure 4c.

We now elaborate on the phase and structural evolution under the optimized synthesis conditions (i.e., ball milling β-$NaFeO_2$ with carbon) to produce disordered rocksalt $NaFeO_2$. *Ex situ* Bragg diffraction measurements were performed to follow the evolution of the rocksalt $NaFeO_2$ as a function of milling time. The diffraction patterns at different stages of synthesis reveal a one-step phase transformation (or two-phase reaction) without any intermediate phase (Figure S6a). Each diffraction pattern was refined using the Rietveld method to estimate the ratio between the reactant (β-$NaFeO_2$) and product (rocksalt $NaFeO_2$) (Figure S6b). The results suggest that ~90% of the initial β-$NaFeO_2$ is transformed into the rocksalt phase after milling for 6 h. In addition, we analyzed the O vacancy concentration of the samples after different milling times by Rietveld refinement. Because at short milling times, the rocksalt phase is not the main phase, the accuracy of the refined occupancy of oxygen is poor. Therefore, we focused on the 5 and 6 h ball milled samples (>70 wt % rocksalt phase is formed) that show O occupancies of 0.95 and 0.94, respectively. These results agree with our conclusion about oxygen vacancy formation during the mechanochemical synthesis and indicate that the O vacancy concentration in the rocksalt structure increases with ball milling time.

To follow the microscopic structural changes of $NaFeO_2$ during the milling process, HRTEM images of the β-$NaFeO_2$ particles after ball milling for 3 h were obtained. At this stage of the transformation, approximately half of the initial β-$NaFeO_2$ was transformed into the rocksalt phase, as observed in Figure S6b, allowing the investigation of both the β and rocksalt structures. The electron diffraction pattern (Figure S3a) of a large particle in this sample (<500 nm) shows both disordered rocksalt and β-$NaFeO_2$ diffraction spots, confirming the coexistence of both phases. Panels a−d of Figure 5 show a particle with a diameter of approximately 200 nm. Upon magnification of the surface of this particle, numerous stacking faults are observed, as indicated by the breaking and shifting of the lattice fringes highlighted in Figure 5c. These stacking faults also appear as diffused spots in the FFT image in Figure 5d.[29] The diffraction pattern of this surface layer (Figure 5d), however, cannot be described by the β, disordered, or ordered rocksalt structure. A smaller particle (~30 nm) in the same 3 h ball milled sample was also examined (Figure 5e−g). The FFT image (Figure 5g) indicated cubic symmetry without any additional cation ordering spots, suggesting that this smaller particle was already transformed into the rocksalt structure.

DISCUSSION

The proposed shear-assisted phase transformation mechanism explains how a β-$NaFeO_2$ structure can transform into an ordered rocksalt structure that would inherit the cation ordering (or γ-$LiFeO_2$ cation ordering) of the starting phase (Figure S7a). Clearly, one of the primary effects of mechanical milling is to reduce the phase-transition barrier through the large shear stress. Note that the shear stress produced during mechanical milling does not have directionality and that only the component of the shear stress that aligns with the energetically favored shear deformation direction has a dominant effect in inducing such a phase transition. However, the shear deformation alone cannot explain the creation of the disordered rocksalt $NaFeO_2$ structure and explain how the zigzag Na−Fe cation ordering from β-$NaFeO_2$ is destroyed (Figure S7). This open question caused us to consider other effects of mechanical milling. We propose that the cation ordering is most likely disrupted by a high concentration of stacking faults produced during milling, as observed at the surface of the $NaFeO_2$ particle (Figure 5), and has also been observed in other mechanical milling processes.[15,30,31] The nature of these stacking faults is unclear. However, because the final rocksalt symmetry is preserved, we expect such stacking faults to retain the anion (or cation) stacking sequence and shift only the relative Na/Fe cation positions in each close-packed layer, similar to the "number stacking faults" proposed by Liu and co-workers.[32] These concentrated stacking faults destroy the long-range three-dimensional coherence of the cation ordering pattern, and thus, no ordering peaks can be observed in the powder Bragg diffraction patterns of the resulting rocksalt phase even though the ordering pattern may still exist locally. The surface layers that are rich in stacking faults (on the order of tens of nanometers) on the initially large β-$NaFeO_2$ particles are expected to detach under mechanical stress because of the lattice mismatch (or strain buildup). The resulting small particles, such as the one shown in Figure 5e, can enable the β-phase-to-rocksalt transformation to occur on the nanometer scale, which is associated with lower energy barriers and is more likely to occur than the transformation of bulk micrometer-scale particles is.

The results obtained in our study of the β-to-rocksalt $NaFeO_2$ phase transformation highlight the effectiveness of shear stress as an additional handle to synthesize inorganic metastable materials in addition to the most commonly used handles of temperature and pressure. Indeed, there are many related reports in the literature[12−14,23,33−36] where the phase transformations induced by techniques that can apply large shear stresses (such as mechanical milling, pressing with a solid medium, and sonication) share common features; that is, the precursor and product are connected via a shear deformation path. Specific examples include the wurtzite-to-rocksalt phase transition of GaN,[23,33] ZnO,[25,35] and CdSe;[26] the rocksalt-to-zincblende transition in SiC;[36,37] and the perovskite-to-postperovskite transition in $CaIrO_3$.[34]

Our study also indicates that the ordered rocksalt structure (γ-$LiFeO_2$ type) is prone to generate stacking faults under mechanical milling and can thus be converted into the disordered polymorph even though local ordering may still exist. Especially with the presence of O vacancies, this process appears to be rather facile. For example, it was recently demonstrated that orthorhombic $LiMnO_2$, which has the same cation ordering as the ordered rocksalt $NaFeO_2$ discussed above, can be transformed into a cation-disordered rocksalt phase when ball milled with Li_2O and carbon.[38] We further show that the same transformation process can also be applied to β-$NaMnO_2$ (space group *Pmnm*), which has a cation ordering similar to that of γ-$LiFeO_2$. After ball milling with carbon for 12 h, the β-$NaMnO_2$ was transformed into a cation-disordered rocksalt structure with a lattice constant of ~4.4 Å (Figure S8). It is worth noting that different alkaline metals and transition metals could make the formation of the disordered rocksalt structure more energetically feasible, thus lowering the requirements for their synthesis conditions (e.g., shear stress, precursor structure, and O vacancies). For example, cation-disordered rocksalt $NaMnO_2$ is 80 meV/atom above the layered ground state compared to 132 meV/atom in the case of $NaFeO_2$, and it was recently synthesized by ball milling the layered $NaMnO_2$.[39] However, the residual layered structure peaks in the XRD pattern suggest that the phase transition is not complete even after ball milling for 36 h. By using β-$NaMnO_2$ as the milling precursor, we were able to complete the phase transformation in <12 h, further demonstrating the importance of the precursor structure. These three cases together, $NaFeO_2$, $LiMnO_2$, and $NaMnO_2$, demonstrate the generalizability of this synthesis method to produce disordered rocksalt phases. These newly synthesized disordered rocksalt materials could have interesting applications as electrodes in secondary batteries because they can potentially mitigate the irreversible structural transformations that often occur in layered materials[16,40] and can activate the anion redox activity, leading to increased capacities.[41,42]

Finally, our study suggests the critical role of tuning the chemical compositions to alter the energetics of competing polymorphs. In our case, via the addition of carbon and thus the creation of O vacancies, the relative energies of different $NaFeO_2$ polymorphs were substantially modified, facilitating the formation of the rocksalt phase. Such stabilization of metastable phases caused by off stoichiometry or slight changes in composition have been observed in many other systems.[8,43] We expect that by evaluating the thermodynamics of the competing phases under various compositions, one can identify the synthesis conditions to selectively stabilize the targeted polymorph.

■ CONCLUSION

Cation-disordered rocksalt $NaFeO_2$ was synthesized for the first time by mechanical milling of β-$NaFeO_2$ with carbon. Using a wide array of bulk and local structural probes, we detected approximately 9% O vacancies in the as-prepared $NaFeO_2$ as well as a significant deviation of the local structure from the long-range averaged structure. The transformation from β-to-rocksalt $NaFeO_2$ was systematically investigated using *ab initio* calculations, X-ray scattering, and electron microscopy. A shear-related precursor structure, shear stress, and O vacancies were all found to be important for such a transformation to occur. Our results should be seen in a broader context of using various thermodynamic handles to stabilize different polymorphs that are then "quenched" back to normal conditions. High temperature and pressure are well accepted as mechanisms for stabilizing phases that have a higher entropy and a smaller volume, respectively, but such a thermodynamic description can be broadened to include size,[44,45] temporary compositional variation,[8] or in our case shear stress as thermodynamic handles. With our understanding of the specific phase transformation process, we were able to predict and synthesize a new cation-disordered rocksalt structure ($NaMnO_2$) and explain the synthesis of several other metastable materials. Furthermore, we propose that mechanochemical synthesis with large shear stresses can be used to trigger phase transformations in which the two end members are connected through shear deformations, motivating the development of computational tools to map structures based on shear deformations and resulting in more predictive synthesis routes.

■ MATERIALS AND METHODS

Synthesis of Cation-Disordered Rocksalt $NaFeO_2$ and $NaMnO_2$. β-$NaFeO_2$ and β-$NaMnO_2$ were first prepared by solid-state synthesis according to the procedures described in previous reports.[18,46] For β-$NaFeO_2$, Na_2O_2 (Sigma-Aldrich, 97%) and Fe_2O_3 (Sigma-Aldrich, 99%) were first mixed by ball milling for 1 h under an Ar atmosphere (5 wt % excess Na_2O_2 was used to compensate for evaporation upon firing). The resulting powder was then pressed into a pellet (12 mm in diameter) and fired in air at 950 °C for 16 h. The pellet was quenched to room temperature, transferred into an Ar-filled glovebox, and ground into a fine powder. Similarly, for β-$NaMnO_2$, Na_2CO_3 (Sigma-Aldrich, 99%) and Mn_2O_3 (Sigma-Aldrich, 99%) were mixed by ball milling for 1 h under an Ar atmosphere (15 wt % excess Na_2CO_3 was used to compensate for evaporation upon firing) and then pressed into a pellet and fired under an oxygen flow at 950 °C for 24 h with a ramping rate of 1 °C/min. The resulting pellet was quenched to room temperature, ground, repressed into a pellet, and fired again under an oxygen flow at 950 °C for 24 h with a ramping rate of 5 °C/min. The sample was again quenched to room temperature, transferred into an Ar-filled glovebox, and ground into a fine powder. The resulting β-$NaFeO_2$ and β-$NaMnO_2$ powders then underwent high-energy ball milling under the same conditions. They were first mixed with graphite (Beantown Chemical, 99.9%) in a 1:1 weight ratio and ball milled at 1060 cycles per minute for 12 h in a SPEX 8000M Mixer/Mill. The milling was performed in a 50 mL ZrO_2 jar with roughly 1 g of a powder mixture and two dozen 5 mm diameter ZrO_2 grinding balls. The 1:1 weight ratio was chosen to achieve best XAS and Mössbauer signals (ideal Fe concentration in the sample). The disordered rocksalt phase still forms under the same milling condition when the carbon weight is reduced to 5%.

XRD and PDF Analyses. The samples for the X-ray scattering measurements were packed into Kapton capillaries (0.0485 inch inner diameter, Cole-Parmer) and sealed with epoxy in an Ar atmosphere. Synchrotron X-ray scattering data were collected on beamline 11-ID-B at the Advanced Photon Source, Argonne National Laboratory, using an X-ray energy of 58 keV ($\lambda = 0.2114$ Å). The X-ray scattering data were integrated using the program Fit2D,[47] and $G(r)$ was obtained using the software PDFGetX2.[48] The PDF data were fitted using PDFGUI ($Q_{max} = 26$).[49] Lab XRD patterns were collected using a Rigaku Miniflex 600 system with Cu Kα radiation. The Bragg scattering data were analyzed using Rietveld refinement with the TOPAS 4.2 software package.

Neutron Scattering. Time-of-flight (TOF) powder neutron diffraction measurements were performed on the Nanoscale Ordered Materials Diffractometer (NOMAD) at the Spallation Neutron Source (SNS) at Oak Ridge National Laboratory. The powder samples were packed and sealed in quartz capillaries (2 mm outer diameter, Hampton Research) under an Ar atmosphere, and each sample was measured for 2 h at room temperature. The Bragg scattering data were analyzed using Rietveld refinement with the TOPAS 4.2 software package.

X-ray Absorption Spectroscopy Analysis. XAS measurements were conducted on the MRCAT 10-ID beamline of the Advanced Photon Source (APS), Argonne National Laboratory. Fe K-edge (7112 eV) spectra were recorded in transmission mode at room temperature with a SiO_2 monochromator, and eight scans were performed to reduce the data noise. The beam size was maintained at 4 mm (horizontal) × 1 mm (vertical). The XAS sample was prepared by rolling a mixture of $NaFeO_2$, carbon, and polytetrafluoroethylene binder into a thin film. The film was sealed with Kapton tape during measurement to avoid air exposure. Reference samples were prepared by mixing sample powders with BN powder and pressing them into 4 mm diameter pellets. The XAS data were analyzed using the Athena and Artemis programs.[50] The extracted EXAFS signal, $\chi(k)$, was weighted by k^3 to emphasize the high-energy oscillation and then Fourier-transformed in a k range from 2.0 to 11.8 Å using a Hanning window to obtain magnitude plots of EXAFS spectra in R-space (angstroms). Data preprocessing operations such as deglitching, energy calibration, normalization, and quantitative analysis of EXAFS spectra with theoretical standards were performed as described by Kelly et al. by using IFEFFIT.[51] Degeneracies, bond distances, and Debye−Waller factors (DWFs) were extracted using nonlinear least-squares fitting procedures in R-space (angstroms).

^{57}Fe Mössbauer Spectroscopy. Zero-field ^{57}Fe Mössbauer spectra were recorded at 295 K with a constant-acceleration spectrometer and a rhodium matrix Co-57 source. Prior to measurements, the instrument was calibrated at 295 K with α-Fe foil. Approximately 20 mg of the as-synthesized $NaFeO_2$/carbon mixture was sealed in plastic O-rings with Kapton tape to avoid air exposure. The Mössbauer spectra were fitted with a sum of symmetric Lorentzian doublets.

Transmission Electron Microscopy. TEM images were obtained using a Philips CM 200 FEG transmission electron microscope operating at 200 kV. $NaFeO_2$ particles were dispersed in ethanol by sonication and then drop casted on an ultrathin carbon film Cu grid. To investigate the phase evolution mechanism, high-resolution images for $NaFeO_2$ after ball milling for 3 and 12 h were collected.

Density Functional Theory Calculations. Ab initio calculations were performed using density functional theory (DFT) with plane wave basis sets as implemented in the Vienna *Ab Initio* Simulation Package (VASP).[52−55] The core electrons were described in the projector augmented wave framework.[56] The generalized gradient approximation with the Perdew−Burke−Ernzerhof (PBE) functional was used for the exchange correlation energy term.[57] A Hubbard U term with a U_{eff} of 4.3 eV was applied on Fe 3d orbitals to compensate for the self-interaction error.[58,59] All the calculations were spin polarized with a ferromagnetic spin configuration.

Solid-State Nudged Elastic Band Calculation. The SSNEB method implemented in the TSASE package was used to calculate the phase-transition pathway, including both the cell and atom degrees of freedom during the transition-state searches.[27] The enthalpy was calculated using the equation $H = E + V\sum_{ij}\sigma_{ij}^{\text{ext}}\varepsilon_{ij}$, where E is the potential energy, σ_{ij}^{ext} is the external stress tensor applied to the system, ε_{ij} is the strain tensor, and V is the deformation volume. Several possible transition paths were calculated, and that with the lowest barrier was selected. An empirical pair potential was trained with the GULP package based on the DFT structures and energies to accelerate the path screening.[60] The potential was of the form defined by Rabani with a short-range Lennard-Jones term and long-range Coulomb term.[61] The potential details are provided in the Supporting Information. The solid-state dimer method was run with this pair potential to automate the search for transition pathways starting from β-$NaFeO_2$.[28] The low-barrier paths were used as initial guesses for DFT-based SSNEB calculations. The reported final paths and barriers are based on the DFT potential-energy landscapes. A 2 × 2 × 1 supercell with 32 oxygen atoms was used for the DFT-based SSNEB calculations. The k-point mesh was 1 × 1 × 3, and the energy cutoff for the plane wave basis set was 520 eV. The generalized forces in SSNEB converged below 0.05 eV/Å.

■ ASSOCIATED CONTENT

Supporting Information

The Supporting Information is available free of charge on the ACS Publications website at DOI: 10.1021/acs.chemmater.8b03490.

> Additional diffraction and TEM data, XRD/XANES fitting parameters, empirical potential, and DFT calculation details (PDF)

■ AUTHOR INFORMATION

Corresponding Authors

*E-mail: shouhang.bo@sjtu.edu.cn.
*E-mail: gceder@berkeley.edu.

ORCID

Tan Shi: 0000-0003-0312-2639
Gopalakrishnan Sai Gautam: 0000-0002-1303-0976
Khetpakorn Chakarawet: 0000-0001-5905-3578

Author Contributions

T.S., S.-H.B., and G.C. designed the experiments. G.C. and S.-H.B. supervised all aspects of the research. T.S. synthesized and characterized (X-ray and neutron scattering, PDF, and XAS) the materials. P.X. performed SSNEB calculations. G.S.G. and P.X. performed DFT calculations. D.-H.K. collected and analyzed TEM data. K.C. acquired and analyzed Mössbauer data. H.K. conducted quantitative analysis of EXAFS data. The manuscript was first written by T.S. and revised by G.C., S.-H.B., P.X., G.S.G., D.-H.K., K.C., and H.K. All authors discussed results and commented on the manuscript.

Notes

The authors declare no competing financial interest.

■ ACKNOWLEDGMENTS

Funding for this study was provided by the U.S. Department of Energy (DOE), Office of Science, Basic Energy Sciences, under Contract DE-AC36-08GO28308 to the National Renewable Energy Laboratory (NREL) as a part of the DOE Energy Frontier Research Center "Center for Next Generation of Materials by Design". Use of the Advanced Photon Source at Argonne National Laboratory was supported by the U.S. Department of Energy, Office of Science, Office of Basic Energy Sciences, under Contract DE-AC02-06CH11357. The TEM experiments were performed at the Molecular Foundry, Lawrence Berkeley National Laboratory, supported by the Office of Science, Office of Basic Energy Sciences, of the DOE (Contract DE-AC02-05CH11231). The neutron scattering experiment was performed at the Spallation Neutron Source (SNS), a national user facility sponsored by the Scientific User Facilities Division, Office of Basic Energy Sciences (BES), DOE. This work used the Extreme Science and Engineering Discovery Environment (XSEDE), which is supported by National Science Foundation Grant ACI-1548562. The authors thank Dr. Jinhyuk Lee, Dr. Wenhao Sun, Dr. Dong-Hwa Seo, Dr. Alexandra Toumar, and Dr. Alexander Urban for helpful discussions. The authors thank Prof. Christopher Chang for the use of the Mössbauer spectrometer in his laboratory and Prof. Gary J. Long and Prof. Fernande Grandjean for advice on the Mössbauer data analysis.

■ REFERENCES

(1) Diercks, C. S.; Yaghi, O. M. The atom, the molecule, and the covalent organic framework. *Science* **2017**, *355*, 923.

(2) Kuech, T. F.; Babcock, S. E.; Mawst, L. Growth far from equilibrium: Examples from III-V semiconductors. *Appl. Phys. Rev.* **2016**, *3*, 040801.

(3) Post, J. E. Manganese oxide minerals: crystal structures and economic and environmental significance. *Proc. Natl. Acad. Sci. U. S. A.* **1999**, *96*, 3447.

(4) Sclafani, A.; Herrmann, J. Comparison of the photoelectronic and photocatalytic activities of various anatase and rutile forms of titania in pure liquid organic phases and in aqueous solutions. *J. Phys. Chem.* **1996**, *100*, 13655.

(5) Jain, A.; Ong, S. P.; Hautier, G.; Chen, W.; Richards, W. D.; Dacek, S.; Cholia, S.; Gunter, D.; Skinner, D.; Ceder, G.; Persson, K. A. Commentary: The Materials Project: A materials genome approach to accelerating materials innovation. *APL Mater.* **2013**, *1*, 011002.

(6) Ong, S. P.; Richards, W. D.; Jain, A.; Hautier, G.; Kocher, M.; Cholia, S.; Gunter, D.; Chevrier, V. L.; Persson, K. A.; Ceder, G. Python Materials Genomics (pymatgen): A robust, open-source python library for materials analysis. *Comput. Mater. Sci.* **2013**, *68*, 314.

(7) Sun, W.; Dacek, S. T.; Ong, S. P.; Hautier, G.; Jain, A.; Richards, W. D.; Gamst, A. C.; Persson, K. A.; Ceder, G. The thermodynamic scale of inorganic crystalline metastability. *Sci. Adv.* **2016**, *2*, e1600225.

(8) Kitchaev, D. A.; Dacek, S. T.; Sun, W.; Ceder, G. Thermodynamics of Phase Selection in MnO2 Framework Structures through Alkali Intercalation and Hydration. *J. Am. Chem. Soc.* **2017**, *139*, 2672.

(9) Kitchaev, D. A.; Ceder, G. Evaluating structure selection in the hydrothermal growth of FeS2 pyrite and marcasite. *Nat. Commun.* **2016**, *7*, 13799.

(10) Badding, J. High-pressure synthesis, characterization, and tuning of solid state materials. *Annu. Rev. Mater. Sci.* **1998**, *28*, 631.

(11) Jayaraman, A. Diamond anvil cell and high-pressure physical investigations. *Rev. Mod. Phys.* **1983**, *55*, 65.

(12) Boldyrev, V. V. Mechanochemistry and mechanical activation of solids. *Russ. Chem. Rev.* **2006**, *75*, 177.

(13) Patel, J.; Cohen, M. Criterion for the action of applied stress in the martensitic transformation. *Acta Metall.* **1953**, *1*, 531.

(14) Dachille, F.; Roy, R. Effectiveness of shearing stresses in accelerating solid phase reactions at low temperatures and high pressures. *J. Geol.* **1964**, *72*, 243.

(15) Gutman, E. M. *Mechanochemistry of solid surfaces*; World Scientific Publishing Co. Inc., 1994.

(16) Yabuuchi, N.; Yoshida, H.; Komaba, S. Crystal Structures and Electrode Performance of Alpha-$NaFeO_2$ for Rechargeable Sodium Batteries. *Electrochemistry* **2012**, *80*, 716.

(17) West, A. NaAlO2 and NaFeO2 polymorphism. *Nature* **1974**, *249*, 245.

(18) Takeda, Y.; Akagi, J.; Edagawa, a.; Inagaki, M.; Naka, S. A preparation and polymorphic relations of sodium iron oxide (NaFeO2). *Mater. Res. Bull.* **1980**, *15*, 1167.

(19) Zakutayev, A.; Zhang, X.; Nagaraja, A.; Yu, L.; Lany, S.; Mason, T. O.; Ginley, D. S.; Zunger, A. Theoretical prediction and experimental realization of new stable inorganic materials using the inverse design approach. *J. Am. Chem. Soc.* **2013**, *135*, 10048.

(20) Proffen, T.; Page, K. L.; McLain, S. E.; Clausen, B.; Darling, T. W.; TenCate, J. A.; Lee, S.; Ustundag, E. Atomic pair distribution function analysis of materials containing crystalline and amorphous phases. *Z. Kristallogr. - Cryst. Mater.* **2005**, *220*, 1002.

(21) Menil, F. Systematic trends of the 57Fe Mössbauer isomer shifts in (FeOn) and (FeFn) polyhedra. Evidence of a new correlation between the isomer shift and the inductive effect of the competing bond TX (→ Fe)(where X is O or F and T any element with a formal positive charge). *J. Phys. Chem. Solids* **1985**, *46*, 763.

(22) Burns, R. G. Mineral Mössbauer spectroscopy: correlations between chemical shift and quadrupole splitting parameters. *Hyperfine Interact.* **1994**, *91*, 739.

(23) Xia, H.; Xia, Q.; Ruoff, A. L. High-pressure structure of gallium nitride: Wurtzite-to-rocksalt phase transition. *Phys. Rev. B: Condens. Matter Mater. Phys.* **1993**, *47*, 12925.

(24) Shimojo, F.; Kodiyalam, S.; Ebbsjö, I.; Kalia, R. K.; Nakano, A.; Vashishta, P. Atomistic mechanisms for wurtzite-to-rocksalt structural transformation in cadmium selenide under pressure. *Phys. Rev. B: Condens. Matter Mater. Phys.* **2004**, *70*, 184111.

(25) Limpijumnong, S.; Jungthawan, S. First-principles study of the wurtzite-to-rocksalt homogeneous transformation in ZnO: A case of a low-transformation barrier. *Phys. Rev. B: Condens. Matter Mater. Phys.* **2004**, *70*, 054104.

(26) Zahn, D.; Grin, Y.; Leoni, S. Mechanism of the pressure-induced wurtzite to rocksalt transition of CdSe. *Phys. Rev. B: Condens. Matter Mater. Phys.* **2005**, *72*, 064110.

(27) Sheppard, D.; Xiao, P.; Chemelewski, W.; Johnson, D. D.; Henkelman, G. A generalized solid-state nudged elastic band method. *J. Chem. Phys.* **2012**, *136*, 074103.

(28) Xiao, P.; Sheppard, D.; Rogal, J.; Henkelman, G. Solid-state dimer method for calculating solid-solid phase transitions. *J. Chem. Phys.* **2014**, *140*, 174104.

(29) Gevers, R.; Van Landuyt, J.; Amelinckx, S. The fine structure of spots in electron diffraction resulting from the presence of planar interfaces and dislocations. *Phys. Status Solidi B* **1966**, *18*, 343.

(30) He, J.; Chung, K. H.; Lavernia, E. J.; Liao, X.; Zhu, Y. T. Mechanical milling-induced deformation twinning in Fcc materials with high stacking fault energy. *Metall. Mater. Trans. A* **2003**, *34*, 707.

(31) Sort, J.; Surinach, S.; Munoz, J.; Baró, M.; Wojcik, M.; Jedryka, E.; Nadolski, S.; Sheludko, N.; Nogués, J. Role of stacking faults in the structural and magnetic properties of ball-milled cobalt. *Phys. Rev. B: Condens. Matter Mater. Phys.* **2003**, *68*, 014421.

(32) Liu, J.; Yin, L.; Wu, L.; Bai, J.; Bak, S.; Yu, X.; Zhu, Y.; Yang, X.; Khalifah, P. G. Quantification of Honeycomb Number-Type Stacking Faults: Application to Na3Ni2BiO6 Cathodes for Na-Ion Batteries. *Inorg. Chem.* **2016**, *55*, 8478.

(33) Limpijumnong, S.; Lambrecht, W. R. Homogeneous strain deformation path for the wurtzite to rocksalt high-pressure phase transition in GaN. *Phys. Rev. Lett.* **2001**, *86*, 91.

(34) Cheng, J.; Zhou, J.; Goodenough, J. Stress-induced perovskite to post-perovskite transition in CaIrO 3 at room temperature. *Phys. Rev. B: Condens. Matter Mater. Phys.* **2010**, *82*, 132103.

(35) Karzel, H.; Potzel, W.; Köfferlein, M.; Schiessl, W.; Steiner, M.; Hiller, U.; Kalvius, G.; Mitchell, D.; Das, T.; Blaha, P.; Schwarz, K.; Pasternak, M. P. Lattice dynamics and hyperfine interactions in ZnO and ZnSe at high external pressures. *Phys. Rev. B: Condens. Matter Mater. Phys.* **1996**, *53*, 11425.

(36) Yoshida, M.; Onodera, A.; Ueno, M.; Takemura, K.; Shimomura, O. Pressure-induced phase transition in SiC. *Phys. Rev. B: Condens. Matter Mater. Phys.* **1993**, *48*, 10587.

(37) Hatch, D. M.; Stokes, H. T.; Dong, J.; Gunter, J.; Wang, H.; Lewis, J. P. Bilayer sliding mechanism for the zinc-blende to rocksalt transition in SiC. *Phys. Rev. B: Condens. Matter Mater. Phys.* **2005**, *71*, 184109.

(38) Freire, M.; Kosova, N.; Jordy, C.; Chateigner, D.; Lebedev, O.; Maignan, A.; Pralong, V. A new active Li-Mn-O compound for high energy density Li-ion batteries. *Nat. Mater.* **2016**, *15*, 173.

(39) Sato, T.; Sato, K.; Zhao, W.; Kajiya, Y.; Yabuuchi, N. Metastable and nanosize cation-disordered rocksalt-type oxides: revisit of stoichiometric LiMnO 2 and NaMnO 2. *J. Mater. Chem. A* **2018**, *6*, 13943.

(40) Bo, S.; Li, X.; Toumar, A. J.; Ceder, G. Layered-to-Rock-Salt Transformation in Desodiated Na x CrO2 (x 0.4). *Chem. Mater.* **2016**, *28*, 1419.

(41) Seo, D.; Lee, J.; Urban, A.; Malik, R.; Kang, S.; Ceder, G. The structural and chemical origin of the oxygen redox activity in layered and cation-disordered Li-excess cathode materials. *Nat. Chem.* **2016**, *8*, 692−697.

(42) Lee, J.; Seo, D.; Balasubramanian, M.; Twu, N.; Li, X.; Ceder, G. A new class of high capacity cation-disordered oxides for rechargeable lithium batteries: Li−Ni−Ti−Mo oxides. *Energy Environ. Sci.* **2015**, *8*, 3255.

(43) Fabris, S.; Paxton, A. T.; Finnis, M. W. A stabilization mechanism of zirconia based on oxygen vacancies only. *Acta Mater.* **2002**, *50*, 5171.

(44) Barnard, A.; Curtiss, L. Prediction of TiO2 nanoparticle phase and shape transitions controlled by surface chemistry. *Nano Lett.* **2005**, *5*, 1261.

(45) Navrotsky, A. Energetics at the nanoscale: Impacts for geochemistry, the environment, and materials. *MRS Bull.* **2016**, *41*, 139.

(46) Billaud, J.; Clément, R. J.; Armstrong, A. R.; Canales-Vázquez, J.; Rozier, P.; Grey, C. P.; Bruce, P. G. *β*-NaMnO2: a High Performance Cathode for Sodium-Ion Batteries. *J. Am. Chem. Soc.* **2014**, *136*, 17243−17248.

(47) Hammersley, A. The FIT2D home page. http://www.esrf.eu/computing/scientific/FIT2D/.

(48) Qiu, X.; Thompson, J. W.; Billinge, S. J. PDFgetX2: a GUI-driven program to obtain the pair distribution function from X-ray powder diffraction data. *J. Appl. Crystallogr.* **2004**, *37*, 678.

(49) Farrow, C.; Juhas, P.; Liu, J.; Bryndin, D.; Božin, E.; Bloch, J.; Proffen, T.; Billinge, S. PDFfit2 and PDFgui: computer programs for studying nanostructure in crystals. *J. Phys.: Condens. Matter* **2007**, *19*, 335219.

(50) Ravel, B.; Newville, M. ATHENA, ARTEMIS, HEPHAESTUS: data analysis for X-ray absorption spectroscopy using IFEFFIT. *J. Synchrotron Radiat.* **2005**, *12*, 537.

(51) Kelly, S.; Hesterberg, D.; Ravel, B.; Ulery, A. L.; Drees, L. R. Analysis of soils and minerals using X-ray absorption spectroscopy. *Methods of Soil Analysis Part 5—Mineralogical Methods* **2008**, *5*, 387.

(52) Kresse, G.; Hafner, J. Ab initio molecular dynamics for liquid metals. *Phys. Rev. B: Condens. Matter Mater. Phys.* **1993**, *47*, 558.

(53) Kresse, G.; Furthmüller, J. Efficient iterative schemes for ab initio total-energy calculations using a plane-wave basis set. *Phys. Rev. B: Condens. Matter Mater. Phys.* **1996**, *54*, 11169.

(54) Kresse, G.; Hafner, J. Ab initio molecular-dynamics simulation of the liquid-metal−amorphous-semiconductor transition in germanium. *Phys. Rev. B: Condens. Matter Mater. Phys.* **1994**, *49*, 14251.

(55) Kresse, G.; Furthmüller, J. Efficiency of ab-initio total energy calculations for metals and semiconductors using a plane-wave basis set. *Comput. Mater. Sci.* **1996**, *6*, 15.

(56) Blöchl, P. E. Projector augmented-wave method. *Phys. Rev. B: Condens. Matter Mater. Phys.* **1994**, *50*, 17953.

(57) Perdew, J. P.; Burke, K.; Ernzerhof, M. Generalized gradient approximation made simple. *Phys. Rev. Lett.* **1996**, *77*, 3865.

(58) Dudarev, S.; Botton, G.; Savrasov, S.; Humphreys, C.; Sutton, A. Electron-energy-loss spectra and the structural stability of nickel oxide: An LSDA U study. *Phys. Rev. B: Condens. Matter Mater. Phys.* **1998**, *57*, 1505.

(59) Dudarev, S.; Botton, G.; Savrasov, S. Y.; Szotek, Z.; Temmerman, W.; Sutton, A. Electronic Structure and Elastic Properties of Strongly Correlated Metal Oxides from First Principles: LSDA U, SIC-LSDA and EELS Study of UO2 and NiO. *Physica status solidi (a)* **1998**, *166*, 429.
(60) Gale, J. D. GULP: Capabilities and prospects. *Z. Kristallogr. - Cryst. Mater.* **2005**, *220*, 552.
(61) Rabani, E. An interatomic pair potential for cadmium selenide. *J. Chem. Phys.* **2002**, *116*, 258.